Chemical Engineering Journal 475 (2023) 146083

Contents lists available at ScienceDirect

Chemical Engineering Journal

journal homepage: www.elsevier.com/locate/cej

Exsolution-enhanced reverse water-gas shift chemical looping activity of $Sr_2FeMo_{0.6}Ni_{0.4}O_{6-\delta}$ double perovskite

Francesco Orsini [a], Domenico Ferrero [a,*], Salvatore F. Cannone [a], Massimo Santarelli [a], Andrea Felli [b], Marta Boaro [b,*], Carla de Leitenburg [b], Alessandro Trovarelli [b], Jordi Llorca [c], Georgios Dimitrakopoulos [d,e], Ahmed F. Ghoniem [d]

[a] Energy Department (DENERG), Politecnico di Torino, Corso Duca degli Abruzzi 24, Torino 10129, Italy
[b] Polytechnic Department of Engineering and Architecture (DPIA), University of Udine, Via Cotonificio 107, Udine 33100, Italy
[c] Institute of Energy Technologies, Department of Chemical Engineering, and Barcelona Research Center in Multiscale Science and Engineering, Universitat Politècnica de Catalunya, EEBE, Eduard Maristany 10-14, 08019 Barcelona, Spain
[d] Department of Mechanical Engineering, Massachusetts Institute of Technology, Cambridge, MA 02139, USA
[e] Exponent, Inc., Natick, MA 01760, USA

ARTICLE INFO

Keywords:
Chemical looping
Perovskite
Exsolution
Core-shell structure
CO_2 reduction

ABSTRACT

This study investigates the structural evolution and redox characteristics of the double perovskite $Sr_2FeMo_{0.6}Ni_{0.4}O_{6-\delta}$ (SFMN) during hydrogen (H_2) and carbon dioxide (CO_2) redox cycles and explores the material performance in the Reverse Water-Gas Shift Chemical Looping (RWGS-CL) reaction. *In-situ* and *ex-situ* X-Ray Diffraction (XRD) and High-Resolution Transmission Electron Microscopy (HRTEM) studies reveal that H_2 reduction at temperatures above 800 °C leads to the exsolution of bimetallic Ni-Fe alloy particles and the formation of a Ruddlesden-Popper (RP) phase. A core–shell structure with Ni-Fe core and a perovskite oxide shell is formed with subsequent redox cycles, and the resulting material exhibits better performance and high stability in the RWGS-CL process. Thermogravimetric (TGA) and Temperature Programmed Reduction (TPR) and Oxidation (TPO) analyses show that the optimal reduction and oxidation temperatures for maximizing the CO yield are around 850 °C and 750 °C respectively, and that the cycled material is able to work steadily under isothermal conditions at 850 °C.

1. Introduction

Anthropogenic greenhouse gases emissions derived from burning fossil fuels contribute to global warming and climate change. According to reports published by the International Energy Agency (IEA) [1], approximately 36.8 Gt of CO_2 were emitted in 2022 from fossil fuel combustion and industrial processes, which is about 0.9% more than in 2021. Renewable Energy Sources (RES) can be used to replace fossil fuels in energy systems, but today RES cannot provide enough base-load electricity and their production is strongly influenced by geographical location [2]. Besides RES, Carbon Capture, Utilisation and Storage (CCUS) can play a pivotal role in reducing emissions during the energy transition [3], along with other measures such as electrification, hydrogen and sustainable biofuels [4]. A promising carbon utilisation strategy is converting CO_2 to synthetic fuels or valuable chemicals, thereby avoiding its emission into the atmosphere, decarbonizing hard-to-abate sectors and storing intermittent renewable energy [5]. In such upgrading processes, CO_2 is typically reduced into CO, being a platform molecule for further downstream synthesis of chemicals.

CO_2 reduction can be achieved *via* thermochemical [6–7], thermocatalytic [8–9], photocatalytic [10] or electrochemical [11–12] conversion. Thermochemical routes apply Chemical Looping (CL) for cyclically splitting CO_2 and/or steam (H_2O) into syngas, a mixture of CO/H_2, making use of solid-state Oxygen Carriers (OCs) [13–16]. Notable examples of current OCs are nonstoichiometric ceria [17–20] and perovskites [21–22] that show fast kinetics and long-term thermochemical stability as compared to stoichiometric oxides. During the thermal reduction (TR) step, the OC releases O_2 thereby generating oxygen vacancies in the lattice. In the subsequent oxidation step, it is re-oxidized when exposed to CO_2/H_2O. Thermochemical cycles structured in this way require relatively high temperatures ($T > 1000$ °C) for TR to take place, implying high energy consumption and potentially

* Corresponding authors.
E-mail addresses: domenico.ferrero@polito.it (D. Ferrero), marta.boaro@uniud.it (M. Boaro).

https://doi.org/10.1016/j.cej.2023.146083
Received 11 June 2023; Received in revised form 8 September 2023; Accepted 14 September 2023
Available online 16 September 2023

subjecting the material to high thermal stresses. A more attractive CL scheme for CO_2 reduction involves the Reverse Water-Gas Shift (RWGS) reaction (Reaction (1)) divided into two steps: H_2-driven reduction (H_2-R) and CO_2-driven oxidation (carbon dioxide splitting (CDS)), making use of suitable OCs such as metal oxides (MeO_x) and perovskites, according to Reactions (2) and (3), respectively.

$$CO_2 + H_2 \leftrightarrow CO + H_2O \quad (RWGS) \tag{1}$$

$$MeO_x + \delta H_2 \rightarrow MeO_{x-\delta} + \delta H_2O \quad (H_2\text{-}R) \tag{2}$$

$$MeO_{x-\delta} + \delta CO_2 \rightarrow MeO_x + \delta CO \quad (CDS) \tag{3}$$

Here, δ stands for the nonstoichiometry of the oxide after reduction. This scheme, referred to as the Reverse Water-Gas Shift Chemical Looping (RWGS-CL), overcomes thermodynamic limitations encountered in the gas phase while operating under milder operating conditions, that is, at lower temperatures (below 900 °C instead of above 1000 °C) than in TR-CDS thermochemical cycles. This is because a strongly reducing agent such as H_2 is used in the loop, thereby reducing the temperature associated with reduction and increasing the CO yield, which is enabled by the higher degree of reduction [23]. Moreover, compared to the conventional RWGS approach [9], a pure CO stream can be produced without other by-products, *e.g.*, CH_4 from CO_2 methanation, since H_2 and CO_2 do not come in contact [24]. This inherent gas separation is a key advantage as the energy demand for product gas treatment can be reduced. Moreover, the syngas composition can be tuned for producing chemicals or liquid fuels.

Perovskite materials find application in several cutting-edge technologies [25], in particular perovskite oxides have been widely explored for CL processes [23,24,26,27]. This family of OCs has a high compositional and structural versatility enabled by tuning the type and amount of dopants into the lattice [28–31]. The dopants and the stoichiometry of the A-site governs the redox behaviour and the structural modifications of perovskites [32], and therefore their oxygen storage properties. Lanthanum ferrites and cobaltites doped with Ca or Sr have been the most investigated and promising systems for RWGS-CL [22,24,26]. Daza et al. [24] studied five strontium-doped lanthanum cobaltites, $La_{1-x}Sr_xCoO_{3-\delta}$ ($0 \leq x \leq 1$ with steps of 0.25) performing H_2 Temperature Programmed Reduction (TPR), CO_2 Temperature Programmed Oxidation (TPO) and isothermal CO_2 conversion experiments. In general, the combination of La-Sr in the A-site resulted in higher yields compared to the undoped perovskites ($x = 0$ and $x = 1$). The initial perovskite phase was not recovered after the reaction; instead, a layered Ruddlesden-Popper (RP) phase of the form $A_{n-1}A'_2B_nX_{3n+1}$ with $n = 1$ was formed and the amount decreased with increasing Sr content. In addition, the importance of the metallic Co active phase was pointed out, which was stabilized with cycles on the layered perovskite support. Two reaction pathways were proposed. The first involves CO_2 adsorption on the layered perovskite, followed by O atom spillover into metallic Co and subsequent dissociation, while the second involves the chemisorption of CO_2 onto the metallic Co with subsequent dissociation. In both mechanisms, the synergy between metallic Co and the RP phase seems to have a relevant role in the observed CO_2 conversion performance. Compared to $LaCoO_3$, lanthanum ferrites ($LaFeO_3$) were found to be more stable, and studies have been focused on investigating the role of doping the B-site in $La_{0.75}Sr_{0.25}Co_{1-y}Fe_yO_3$ ($y = 0$, 0.5, 0.75, 1) with the aim of lowering the cycle temperatures while running the process under isothermal conditions, thereby reducing the materials' requirements and the heat losses [33].

Under reducing conditions, doped perovskites can exsolve metallic nanoparticles from the B-site [34–36]. This leads to the decoration of the perovskite surface with metallic catalysts able to promote the adsorption and activation of reactants [37]. The benefits of the exsolution process are well known in many applications [38] such as electrocatalysis [39], catalysis [40–41] and membrane reactors [42], but not yet extensively studied in CL applications. Indeed, relatively few works were reported so far concerning exsolution-enhanced CL processes, with a share including Partial Oxidation of Methane (CLPOM) [43–45], Dry Methane Reforming (CLDMR) [46], and Steam Methane Reforming (CLSMR) [47]. Similarly, no previous works studied extensively the exsolution-enhanced RWGS-CL process. The Fe-Co or Ni-Fe alloys formed by this process appear to catalyse both the reduction and oxidation phases [36]. Iron would favour the desorption of CO during the oxidation step and Ni and Co could support the activation of H_2 in the reduction step [48]. According to the literature, some of the most promising perovskite oxide OCs are multi-phase systems where it was possible to stabilize a non-stoichiometric perovskite with high oxygen vacancy concentration with metal/metal oxide nanoparticles that promote reversible redox cycles. In a recent work, a core–shell Co_3O_4-NiO@$La_{1-x}Sr_xFeO_3$ was engineered, in which the shell of perovskite enhanced the oxygen storage capacity of the metal oxides phases [49]. The main drawbacks of perovskite oxides as OCs include the drop in product yield with cycling attributed to the occurrence of structural changes that hinder the reversibility of the redox process or due to slow oxidation kinetics which leads to a nonstoichiometric oxide [16,21,24,26]. Some authors have also reported the poisoning effect of CO_2 which tends to form carbonates. High temperature *in-situ* XRD of $BaCo_{0.4}Fe_{0.4}Zr_{0.2}O_{3-\delta}$ was performed by Efimov et al. [50], and experiments showed the formation of 29 $\%_{wt}$ of $BaCO_3$ at 900 °C with 50 $\%_{vol}$ CO_2/N_2.

Supported perovskites [51–53] and new compositions were considered in order to address stability concerns. Recently, a double perovskite La_2NiFeO_6 was investigated. Using this material, CO production, averaged over five cycles, of 2.14 mmol/g, and a maximum rate of 1.69 mmol/g min were obtained at 700 °C. Such values correspond to a CO production of 4.7-fold and a rate of production of 10-fold higher than those obtained from the single $LaNiO_3$ and $LaFeO_3$ and confirmed the synergistic action of Ni and Fe in promoting high reducibility and CO_2 splitting activity [48]. In general, double perovskites $AA'B_2X_6$ (or $A_2BB'X_6$) [54] and RP perovskites ($A_{n+1}B_nX_{3n+1}$) [55], as a layered derivative of the perovskite structure, expand the chemical and structural space of perovskite family. Thanks to their higher tuneability in structures and compositions, these subclasses of perovskite provide enhanced and unique options for the design of solid oxides with peculiar electronic configurations and a great variety of physicochemical properties with relevant applications in the field of energy.

In view of identifying new double $AA'BB'O_6$ perovskites as OCs for the RWGS-CL process, the present work investigates the behaviour of $Sr_2FeMo_{0.6}Ni_{0.4}O_{6-\delta}$ (SFMN). $SrMMoO_6$ (M = Mg, Ti, Ni, Fe) and in particular Sr_2FeMoO_6 have been extensively studied for their magnetic properties [50–54] since the different arrangement of (M)FeO_6 and MoO_6 can implement different electronic and magnetic properties. Coordinated Fe-O-Mo combinations by introducing Fe^{2+}-Mo^{6+} and Fe^{3+}-Mo^{5+} redox pairs and oxygen vacancies for charge balancing also play an important role in increasing oxygen defects and improving oxygen transport. This broadens the range of application of these types of double perovskites. They have found many applications as anode and cathode electrodes in solid oxide cells (SOCs) [56–60] and to a lesser extent in catalysis [61–62]. In the former application, these materials possess tunable properties which depend on their composition [63–64] and on the type of dopants in the A and B sites [65–66]. They generally show high electronic and ionic conductivity [56], considerable resistance to carbon and sulfur poisoning [65] and good redox thermal and mechanical stability. Ni-doped Sr_2FeMoO_6 perovskites were reported to easily exsolve Ni particles by forming a multiphase system consisting of an RP phase, a perovskite-like phase and Ni-Fe alloy particles embedded in the perovskite matrix [67]. This multiphase material was shown to be very active in CO_2 electrolysis [68–70]. With exsolution, other types of systems (Ni-$Sr_2Fe_{1-x}Mo_xO_6$) have been engineered to obtain symmetric or reversible SOCs electrodes [71]. Ni-doped Sr_2FeMoO_6 may have interesting properties in CL applications especially in the presence of sulfur impurities, compared to the state of the art on OCs. To the best of our knowledge, our study is the first to investigate the properties of

SFMN in thermochemical redox cycles and under RWGS-CL conditions, thereby contributing to explore more in detail the performance-enhancing role of exsolution in CL processes.

To assess the properties of SFMN during RWGS-CL, Thermogravimetric Analysis (TGA) experiments were performed. A characterization of the structural changes and the exsolution process under redox cycles was performed by means of X-Ray Diffraction (XRD), High-Angle Annular Dark Field Scanning Transmission Electron Microscopy (HAADF-STEM), Energy-Dispersive X-ray (EDX) analysis, High-Resolution Transmission Electron Microscopy (HRTEM) and Temperature Programmed Reduction/Oxidation (TPR/TPO) analyses. Finally, a long-term test was performed in a laboratory microreactor to confirm the stability of this material.

2. Materials and methods

2.1. Material synthesis

SFMN powders were prepared using a citrate auto-combustion route. $Sr(NO_3)_2$, $Fe(NO_3)_3$, $(NH_4)_6Mo_7O_{24}{\cdot}4H_2O$, and $Ni(NO_3)_2{\cdot}6H_2O$ (Sigma Aldrich, purity $\geq$ 99%) were separately dissolved in distilled water. To avoid possible inhomogeneous precipitation the nitrate solutions of Sr, Fe and Ni were mixed and stirred for 15 min before adding Mo solution. Citric acid (CA) was employed as the complexing agent, with a citric acid-to-cations molar ratio of 2:1. After the addition of the CA, the pH was adjusted to 8 using an ammonium hydroxide solution (30%). The solution was then stirred and dried at 80 °C for 24 h. The temperature of resulting gel was set to 350 °C to allow auto-ignition, and the powders were then collected and finely ground in an agate mortar and calcinated at 1100 °C for 10 h, with a heating ramp of 10 °C/min. The amount of Ni in the synthesized sample was confirmed by Inductively Coupled Plasma Mass Spectrometry (ICP-MS), showing 4.9 $\%_{w/w}$ very close to the nominal value 5.5 $\%_{w/w}$.

2.2. Characterization methods

X-ray Diffraction (XRD) was performed using a Philips PW3040/60 X'Pert PRO diffraction system, with Bragg-Brentano geometry, using a Cu Kα radiation (40 kW, 40 mA, $\lambda = 0.154$ nm). The data were acquired at 0.02° at a counting time of 40 s/step in the 20–80° 2θ range. References data [67,72] and a search-match method [73] based on the JCPDS database were used to identify the crystalline phases in the as-synthesized and tested samples.

An *in-situ* X-ray diffractometric structural characterization was performed using an Anton PAAR hot-chamber-XRK 900 (HC-XRD). Each acquisition was done at 0.02° at a counting time of 15 s/step. It consisted in two diffractograms, the first in the range 19–39° 2θ to follow perovskite structural changes, the second in the range 42–54° 2θ to observe the exsolution of Ni and the formation of Ni-Fe alloy (see SI and Fig. S1 for further details).

HAADF-STEM, HRTEM and EDX analysis were performed on a FEI Tecnai G2 F20 instrument equipped with a field emission gun operating at an accelerating voltage of 200 kV.

TPR and TPO analyses were performed with an Autochem II 2920 Micromeritics Analyzer equipped with a thermal conductivity detector (TCD) and mass spectrometer (Omnistar 300). TGA (STA 2500 Regulus, Netzsch, Germany) was conducted on SFMN perovskite samples to evaluate the redox performance in terms of CO production in thermochemical cycles when CO_2 is used as the oxidizing gas.

A tubular fixed-bed reactor was used to evaluate the stability of the material. Mass Flow Controllers (Brooks Instrument, USA) were used to control the gas flow mixture. The sample powder was dispersed in a quartz wool and placed in the centre of an alumina tube positioned inside a tubular furnace (Carbolite Gero, Germany). A multichannel (NDIR/UV/TCD) gas analyser (X-Stream XE, Emerson, USA) was used to measure the concentration of gases (CO, CO_2, H_2) at the outlet of the reactor.

3. Results and discussion

3.1. Morphological and structural characterization of SFMN

The SFMN powder prepared by citrate auto-combustion route has a surface area of 2 m^2/g. XRD analysis (Fig. S2a) depicts the presence of a single-phase perovskite with a cubic crystal structure without evidence of additional phases, thus confirming the formation of the double perovskite and the incorporation of Ni into its lattice.

3.2. Thermochemical cycles and characterizations

Several experimental tests and *in-situ* and *ex-situ* characterizations were carried out to study the redox behavior of SFMN and the impact of its structural changes during the RWGS-CL process.

3.2.1. Thermogravimetric RWGS-CL tests

Systematic TGA experiments were conducted to study the influence of reduction and oxidation temperatures on CO yield during RWGS-CL cycles. Three samples with different masses were used, each of which was placed in a cylindrical crucible made of alumina (Al_2O_3), and a constant gas volumetric flow rate of 225 Nml/min was applied. Blank runs confirmed that the actual mass variations were preserved during the tests. The samples were heated up to the desired temperature at a constant rate of 20 °C/min in an inert Ar atmosphere. Reduction was conducted with 2.7% H_2/Ar for 30 min and at constant temperature. The subsequent oxidation was performed in an anhydrous environment composed of 20% CO_2/Ar for 15 min. The system was purged with pure Ar before and after each step of the cycle for 10 min and during all temperature ramps. Sample mass was maintained low (less than 1 mg) to ensure a uniform and complete reaction throughout. The TGA experiments are summarized in Table 1. Each sample was tested 3 times for each combination of T_{red} and T_{oxy} reported in the table. The experiments were performed in the order reported in Table 1, starting from sample #1 cycled the first time at $T_{red} = 550$ °C and $T_{oxy} = 550$ °C, then at $T_{red} = 550$ °C and $T_{oxy} = 650$ °C and then proceeding in the order of increasing the oxidation temperature, up to the combination $T_{red} = 550$ °C and $T_{oxy} = 950$ °C. Finally, the reduction temperature was increased at $T_{red} = 650$ °C and the sequence repeated. Sample #2 and #3 were tested following similar procedure.

In this way, it was possible to compare the CO production for each reduction–oxidation temperatures pair between 550 and 950 °C. A total of twenty-five temperature combinations tests using three identical cycles for each of them were performed.

TGA oxidation curves are shown in Fig. S3-7. The sample behaviour during oxidation changes as the temperature increases. Reducing at 550 °C or 650 °C (Fig. S3-4, respectively) leads to unstable oxidation profiles: a non-monotonic increase then decrease of mass variation is observed at $T_{red} = T_{oxy} = 550$ °C and at $T_{red} = 650$ °C, $T_{oxy} = 550$ °C (Fig. S3a and S4a, respectively); the measured mass did not reach a stable and repeatable plateau in the 3 redox cycles.

In the first test (that is, reduction at 550 °C and 650 °C – Figs. S3-S4), for 3 temperature combinations out of 10 the mass gain increases from cycle 1 to cycle 3, while it decreases in 6 cases out of 10 (with a

Table 1
Summary of thermogravimetric RWGS-CL tests.

Sample #	Mass (mg)	T_{red} (°C)	T_{oxy} (°C)
1	0.810	550	550 – 650 – 750 – 850 – 950
		650	550 – 650 – 750 – 850 – 950
2	0.835	750	550 – 650 – 750 – 850 – 950
		850	550 – 650 – 750 – 850 – 950
3	0.899	950	550 – 650 – 750 – 850 – 950

maximum difference – negative – of the mass gain around 47% from cycle 1 to 3 at T_{red} = 550 °C, T_{oxy} = 850 °C – see Fig. S3d). An overall decrease in mass during oxidation is observed at Tred = 550 °C, T_{oxy} = 950 °C (Fig. S3e), suggesting that the material may be unstable or requires a longer stabilisation time under such operating conditions.

Reducing at 750 °C and 850 °C (that is, the second group of experiments – Figs. S5-S6, respectively) results in a different behaviour. Fig. 1a shows the three complete redox cycles performed at T_{red} = 850 °C, T_{oxy} = 750 °C. In all cases, the mass gain increases monotonically. The mass reaches a plateau, except at relatively low oxidation temperatures at which complete oxidation is not achieved. This happens at T_{red} = 750 °C, T_{oxy} = 550 °C (Fig. S5a); T_{red} = 850 °C, T_{oxy} = 550 °C (Fig. S6a); T_{red} = 850 °C, T_{oxy} = 650 °C (Fig. S6b). Best cyclic repeatability is seen at T_{red} = 850 °C, T_{oxy} = 750 °C (Fig. 2a and Fig. S6c – negative difference in the main gain values around 1.4% from cycle 1 to 3).

Reducing at 950 °C (that is, the third experiment shown in Fig. S7) leads to a complete oxidation at the corresponding oxidation temperature, and good repeatability for T_{oxy} = 750 – 950 °C (Fig. S7c-e); the difference of the mass gain is below 4% from cycle 1 to 3. Complete oxidation is not achieved for T_{oxy} = 550–650 °C (Fig. S7a-b, respectively).

Fig. 1b shows the averaged oxidation curves at T_{red} = 750–850 °C (that is, the average of the three repetitions for each cycle). The overall mass gain increases for higher T_{red} at a given T_{oxy}, because of the higher oxygen release during the corresponding reduction phase which creates more oxygen vacancies in the lattice and thus a higher CO production. The CO yield (average of the three cycles) for different reduction and oxidation temperatures is reported in Fig. 2. Results at T_{red} = 550 °C are not shown. According to this data, the optimal T_{oxy} range is between 650 and 750 °C, whereas the optimal range for T_{red} is between 850 and 950 °C. The average yield, calculated over the different oxidation temperatures, increases monotonically with the reduction temperature from $T_{red} \geq 650$ °C. Since this increase from T_{red} = 850 °C to T_{red} = 950 °C is less than 3%, a reduction temperature around 850 °C is optimal because of the lower energy requirements. An exergy analysis at reactor and system levels is required to identify the optimal conditions of the process, which is out of the scope of the present material-performance focused work.

3.2.2. *In-situ and ex-situ structural characterization*

In order to explain the results of the TGA experiments, structural changes experienced by the material during reduction and oxidation at increasing temperatures were studied with *in-situ* XRD. The highest temperature of *in-situ* XRD was limited to 850 °C because of operating temperature constraints of the hot chamber, and hence, the structural evolution of the material after reduction at 900 °C was instead studied *ex-situ*. The temperature ramp rate was fixed at 10 °C/min, with a constant volumetric flow rate of 38 Nml/min. TPR was run in 5% H_2/N_2, whereas TPO in 20% CO_2/He. Diffractograms were recorded at the reference temperature of 50 °C and then at 550 °C after 30 min, at 650 °C after 30 min, at 800 °C after 1 h and at 850 °C after 10 min. In order to clearly identify the changes after reduction, three reduction ramps were repeated before running the oxidation ramp (see Fig. S1).

Fig. 3 presents the diffraction profiles obtained after the first out of three reduction steps. The initial SFMN diffractogram showed peaks at 25° 2θ and 27.7° 2θ (Fig. 3a) attributable to segregated impurities of $SrCO_3$ and $SrMoO_4$ respectively [74], which could have been formed before the test (the sample was exposed to air for several months after synthesis and before being tested). However, these phases disappeared above 650 °C while a peak at 30.6° 2θ corresponding to the formation of Sr_3MoO_6 became visible. Since $SrCO_3$ is stable in air up to 900 °C [75], it is likely that the reducing atmosphere favored the strontium carbonate decomposition and the reincorporation of strontium back into the lattice of $SrMoO_4$ according to the following reaction [74]:

$$SrMoO_4 + 2SrCO_3 \leftrightarrow Sr_3MoO_6 + 2CO_2 \quad (4)$$

As the temperature was raised to 800 °C, the main peak related to the double perovskite shifted to the left and widened. At 850 °C a clear shoulder became visible and kept growing with the extent of reduction.

Fig. 4a shows the results of three consecutive reduction steps and highlights the development of a new peak due to the formation of an RP phase identified as $Sr_3FeMoO_{7-\delta}$ [67].

Fig. 3b and Fig. 4b show the changes in the 2θ range of 43-53°, where the (1 0 0) peak corresponding to the metallic cubic phases Ni_3Fe is expected to arise at 44.5° 2θ [67]. This peak was observed (shifted at 43.8° 2θ due to thermal effects) when the reduction temperature reached 800 °C, and it continued to broaden with the sequential reduction steps (inset in Fig. 4b) because of the contribution of the contiguous peak related to the (2 0 0) peak of the RP phase. This shows that thermal treatments in the reducing atmosphere caused a progressive structural transformation of SFMN.

The final transformation achieved at temperature above 850 °C was examined by *ex-situ* characterizations. Fig. S2b shows XRD results related to structural changes of SFMN after four TPRs with temperatures up to 900 °C. We observed the formation of a layered RP phase of composition $Sr_3FeMoO_{7-\delta}$ and a perovskite-like phase of composition $Sr_2Fe_{1-x}Mo_xO_{6-\delta}$, along with the formation of a Ni-rich alloy, which is in agreement with previous reports [67]. Fig. 5 shows that the sample after the fourth TPR contains round-shaped particles embedded in a matrix with diameter in the range of 20–50 nm. The areas marked by green and orange rectangles were characterized using the EDX and their corresponding spectra are shown in the image along with the identification of the elements present (the Cu signals do not correspond to the sample and originate from the TEM grid). The green spectrum, which is taken in an area occupied by a round-shaped particle, shows peaks of Ni and Fe (in accordance with the existence of Ni_3Fe). The orange spectrum, which corresponds to the matrix, shows peaks of Sr, Mo and Fe (in accordance

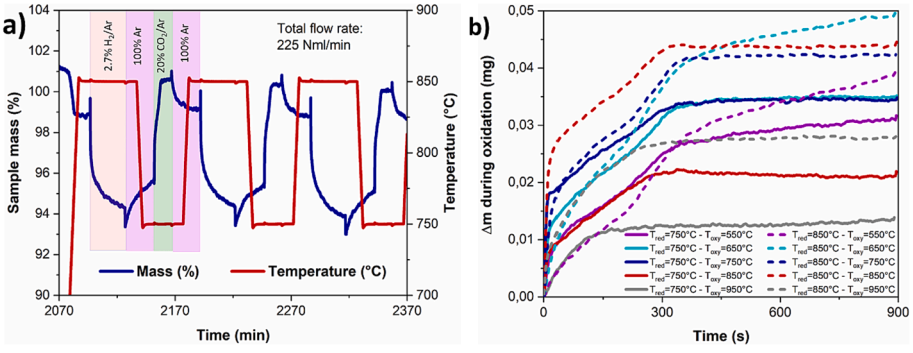

Fig. 1. (a) Representative thermograms from TGA at T_{red} = 850 °C, T_{oxy} = 750 °C. Total flow rate of 225 Nml/min – Reduction in 2.7% H_2/Ar – Oxidation in 20% CO_2/Ar. (b) Cycle-averaged oxidation profiles from TGA for T_{red} = 750 and 850 °C.

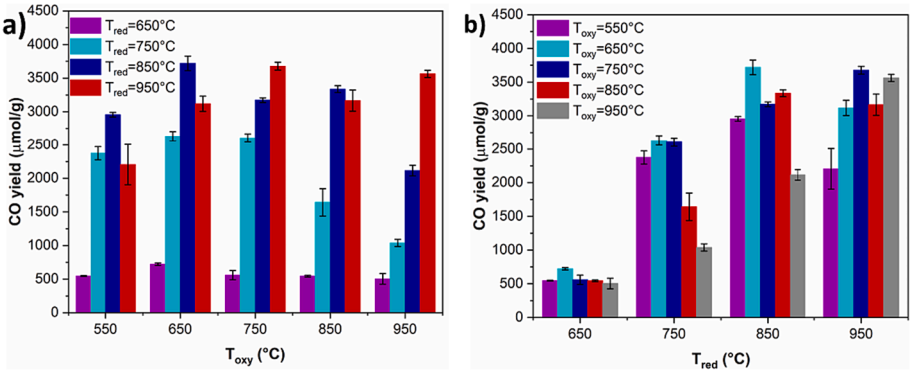

Fig. 2. CO specific yields (3-cycles-averaged values) as function of (a) reduction and (b) oxidation temperatures. Results for $T_{red} = 550$ °C are not shown due to high instability.

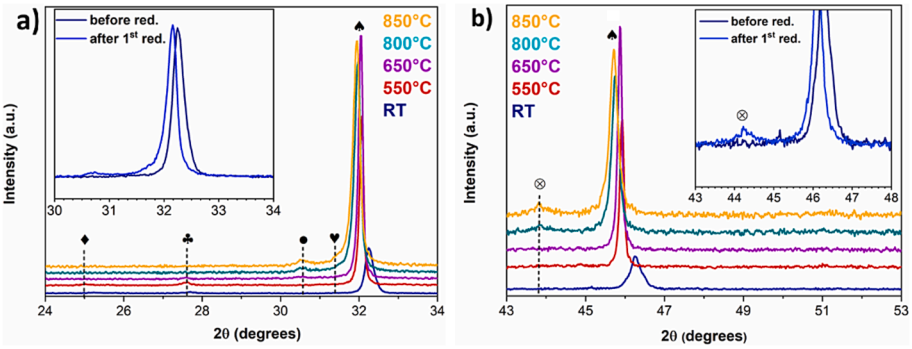

Fig. 3. *HC-XRD analysis during the first reduction step in 5% H_2/N_2 (a) in the range 24–34° 2θ and (b) in the range of 43–53° 2θ. $SrCO_3$ (◆), $SrMoO_4$ (♠), Sr_3MoO_6 (•), RP phase $Sr_3FeMoO_{7-\delta}$ (♥), Sr_2FeMoO_6 (♠), Ni-Fe (⊗). Insets in (a) and (b): diffractograms at room temperature.*

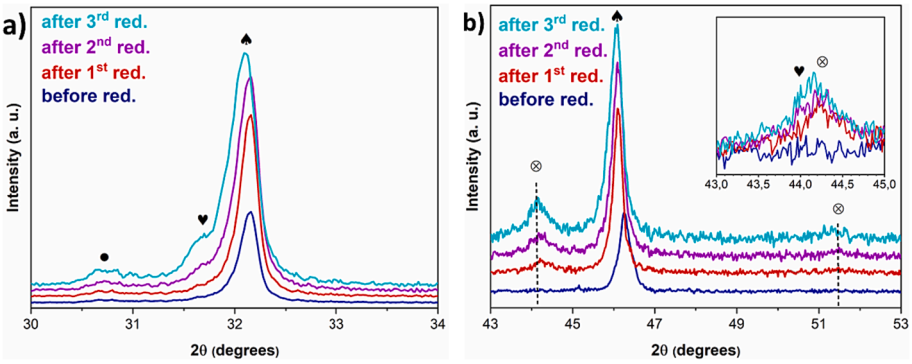

Fig. 4. *HC-XRD analysis before and after consecutive reduction ramps in 5% H_2/N_2 (a) in the range of 30–34° 2θ and (b) in the range of 43–53° 2θ. Sr_3MoO_6 (•), RP phase $Sr_3FeMoO_{7-\delta}$ (♥), Sr_2FeMoO_6 (♠), Ni-Fe (⊗).*

with the presence of the perovskite). HRTEM images allow the identification of the phases present in the material. Lattice fringes are present for both the matrix and the round-shaped particle which means that the sample is crystalline. The lattice fringe at 2.8 Å from the matrix corresponds well to the (2 2 0) crystallographic planes of Sr_2FeMoO_6 and to the (1 0 0) planes of $Sr_3FeMoO_{6.5}$. The lattice fringe at 2.0 Å of the round-shaped particles corresponds to the (1 1 1) crystallographic plane of the Ni-Fe alloy. Here, the Fourier Transform (FT) image corresponding to the interior of a round-shaped particle is also included. Spots at 2.0 and 1.8 Å correspond well to the (1 1 1) and (2 0 0) planes of Ni-Fe alloy, indicating the particle is oriented along the [1 1 0] crystallographic direction. It should be also noted that the round-shaped particles are covered by a thin 2–3 nm layer with 2.4 Å lattice fringes, most likely corresponding to a Ni-Fe oxide (crystallographic planes of NiO (1 1 1) are at 2.4 Å) formed upon handling the sample in air, though being also compatible with the formation of a perovskite oxide layer.

Fig. 6 depicts the results of the *in-situ* HC-XRD tests during the TPO step in CO_2. The shoulder associated with the RP phase disappeared as the temperature increased above 650 °C while the metallic phase remained visible. No peaks of the oxidized Ni phase at 37.26° 2θ (1 1 1) and 43.29° 2θ (2 0 0) are present (JCPDS #04–0835). In addition, for all temperatures investigated herein, we observed the appearance of $SrCO_3$ and $SrMoO_4$ segregated phases. These latter should be formed from Sr_3MoO_6 and CO_2 according to the equilibrium in Equation (4). Thus, CO_2 is able to oxidize the perovskite-like phases (RP phase and $Sr_2Fe_{1-x}Mo_xO_{6-\delta}$) forming a double perovskite phase, but the exsolution process is irreversible and Ni remains exsolved in its metallic phase, since CO_2 is not able to oxidize the metallic Ni.

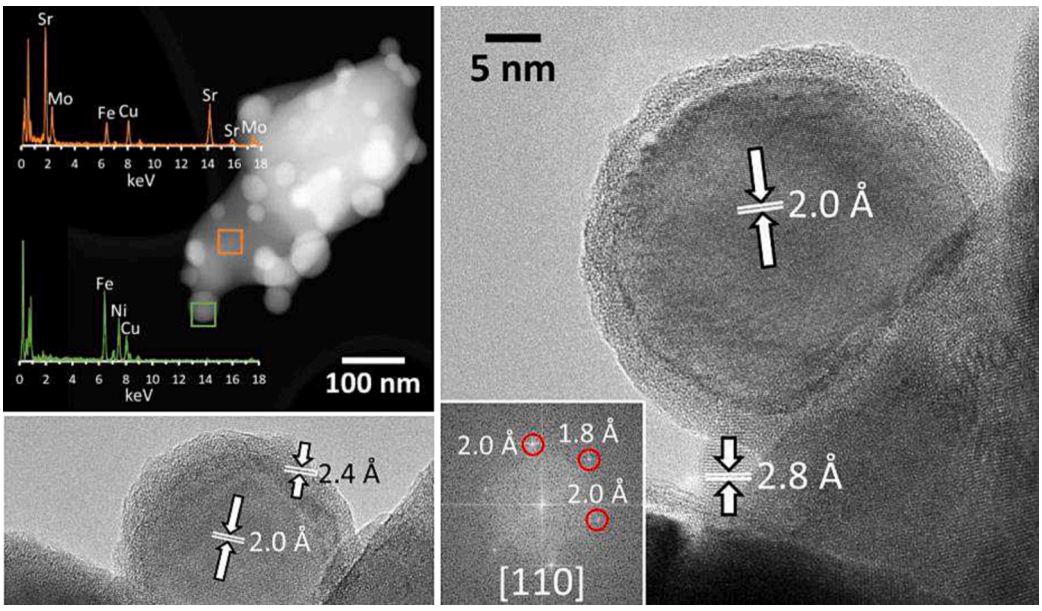

Fig. 5. HAADF-STEM (left-top) and HRTEM images (bottom left and righ, same scale) of a reduced SFMN sample after 4 TPRs in 5% H_2/N_2 (10 °C/min, 35 Nml/min). TPRs preceded by an oxidation step at 500 °C in air for 1 h (35 Nml/ min). The EDX analysis shown in the STEM image refers to the square areas (the green square corresponds to an exsolved particle, the orange square identifies a crystalline area of SFMN with no particles present. (For interpretation of the references to colour in this figure legend, the reader is referred to the web version of this article.)

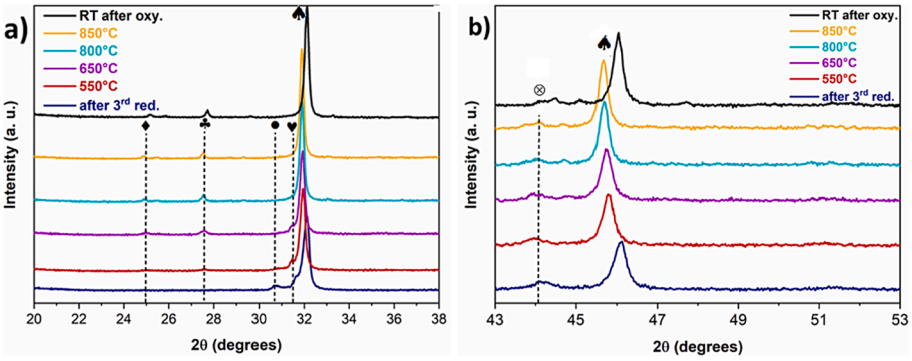

Fig. 6. *HC-XRD analysis during the oxidation ramp in 20% CO_2/He after three ramps of reduction up to 850 °C (a) in the range 20–38° 2θ and (b) in the range 43–54° 2θ. $SrCO_3$ (◆), $SrMoO_4$ (♣), Sr_3MoO_6 (●), RP phase $Sr_3FeMoO_{7-\delta}$ (♥), Sr_2FeMoO_6 (♠), Ni-Fe (⊗).*

Based on TGA and XRD characterization, we conclude the following:

i. The unstable response observed at low reduction temperatures (550–750 °C) can be attributed to poor and slow reduction, likely only occurring at the surface of the sample [76]. TPR results of the pristine SFMN are in agreement with this conclusion (see section 3.2.3). At low temperatures, the structural changes associated with the reduction process take a very long time to complete, so successive thermograms are affected by the slow transformation of the material, resulting in unproducible signals.
ii. The more stable performance observed for reduction and oxidation temperatures in the range of 850–950 °C is related to a complete reduction followed by oxidation of the material associated with the irreversible exsolution of Ni_3Fe nanoparticles and the formation of a highly oxygen deficient RP phase.
iii. The optimal temperature for oxidation (650–750 °C) corresponds to the temperature required for the oxidation of the RP phase (see Fig. 6). Here, the lag in stabilizing the mass signal can be due to a slow accumulation of carbonates and/or the co-presence of phases with slower oxidation kinetics.

In addition, with the concomitant formation of carbonates under oxidizing conditions, it is possible that the CO yield data coming from the TGA were overestimated. Mass variations due to reoxidation of the sample could have been overestimated for up to around 1–1.5% (see more details in the SI), leading to rescaling the CO production from ≈ 3300 μmol/g to ≈ 2700 μmol/g in the isothermal cycles at 850 °C.

3.2.3. Temperature Programmed Reduction (TPR) and Oxidation (TPO) cycles

TPR and TPO cycles were performed to better understand the effect of the phase transformation and exsolution on H_2-reduction and CO_2-oxidation steps of RWGS-CL cycles.

A TPR was performed from room temperature up to 850 °C (heating ramp at 10 °C/min) in 5% H_2/N_2 and volume flow rate fixed at 35 Nml/min. This temperature was chosen from the previous characterization in which exsolution was found to occur for T > 800 °C. Once the target temperature was reached, the sample was kept at 850 °C for 1 h in the same reducing atmosphere. After the cooling ramp to room temperature was completed, a TPO was carried out under the same previous conditions but in an oxidizing atmosphere of 20% CO_2/He. This cycle was then repeated to assess the influence of structural changes on reduction

in terms of H_2 consumption, while examining the reversibility of the redox process by comparing H_2 consumption and CO production. Results of the test are shown in Fig. 7 and Fig. S8. The TPR profile of the first cycle (top-left, red profile) shows two overlapping valleys in the range of 200–500 °C, followed by drop within 550–750 °C. Based on literature reports [63,70,77] and the *in-situ* XRD characterization carried out in this study, these features can be attributed to the following processes:

i. Removal of surface oxygenated species (carbonates) and reduction of surface reducible cations Ni(II) to Ni(0) and Fe(IV) to Fe (III) in the temperature range of 200–350 °C;
ii. Reduction of Fe(III) to Fe(II), Ni(II) to Ni(0) and Mo(VI) to Mo(IV) or Mo(V) in the bulk of the double perovskite with concomitant structural transformations (formation of RP phase and Ni exsolution), in the range of 400–750 °C;
iii. Reduction of Fe(II) to Fe(0) above 750 °C [63].

Different shape and locations of the valleys can be observed in the TPR profile (top right profile) of the second redox cycle. Here, the two main features move towards higher temperatures, while the band centered at around 700 °C disappears. In addition, there is higher consumption of H_2, with a 30% increase from 66 Nml/g in the first cycle to 85 Nml/g in the second cycle. This change corresponds almost to the complete reduction of Ni in the sample. Since reduction is linked to structural changes involving the exsolution of Ni-Fe nanoparticles, we can assume that the difference in the shape of the TPR profiles is indicative of exsolution. The exsolution has a beneficial effect on the reduction since it leads to the formation of perovskite-like structures more prone to reduction. The oxidation with CO_2 occurs in the range 550–750 °C with a maximum CO production at 650 °C in both cycles. The yield of the redox process, defined here as the ratio between the CO produced in [Nml/g_{SFMN}] and the H_2 consumed in [Nml/g_{SFMN}], is ~ 1.16 and ~ 1.04 in the first and second cycle, respectively. This shows that CO_2 is able to fully re-oxidize the SFMN perovskite in the operating conditions investigated, and that the CO production depends on the degree of reduction of the material. It is worth noting that in each of the two oxidation steps, the onset and position of the CO peak remain unchanged, thus providing no information on the impact of exsolution on oxidation kinetics. The XRD results (Fig. 4b) show that a partial dissolution of Ni already occurred during the first reduction, so the similarity in the onset temperature of the two consecutive TPO can be explained by the activation of CO_2 by the partially exsolved Ni already during the first cycle.

In order to evaluate the effect of exsolution on the oxidation step, CO production was carefully evaluated before and after 550 °C, the temperature below which we did not observe significant exsolution in our experimental study. In total, thirteen redox cycles were performed. Each of the first eleven cycles consisted of the following steps: (i) TPR with 35 Nml/min of 5% H_2/N_2 from room temperature to 550 °C (temperature ramp at 10 °C/min), followed by 30 min at constant temperature in the same reducing atmosphere; (ii) purging step of 15 min in He at the same temperature; (iii) oxidation step for 30 min with 35 Nml/min in 20% CO_2/He; (iv) cooling down to room temperature. In the twelfth cycle, the sample was reduced in the same reducing atmosphere from room temperature to 850 °C and was kept at this temperature for 1 h, oxidized for 30 min and then cooled down in He. Finally, the thirteenth cycle was performed in the same way as the first eleven cycles (that is, isothermal cycle at 550 °C). Selected results of this test are shown in Fig. 8. The beneficial effect of exsolution on the oxidation step is demonstrated by comparing the material performance at lower temperature (for example, at 550 °C) before and after its reduction at 850 °C during the twelfth cycle (exsolution was prominent at this temperature as determined through the previous tests). The thirteenth cycle showed a yield of 0.8, whereas the first eleven cycles yielded 0.3 on average. This

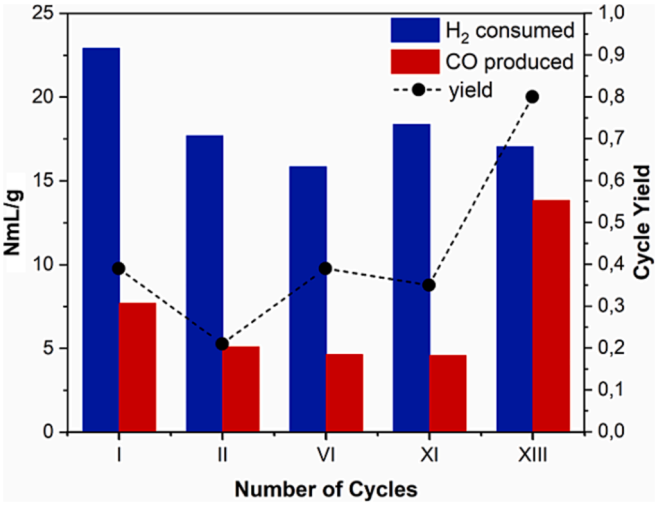

Fig. 8. Quantitative results of selected isothermal cycles carried out at 550 °C, 13th cycle preceded by a cycle at 850 °C.

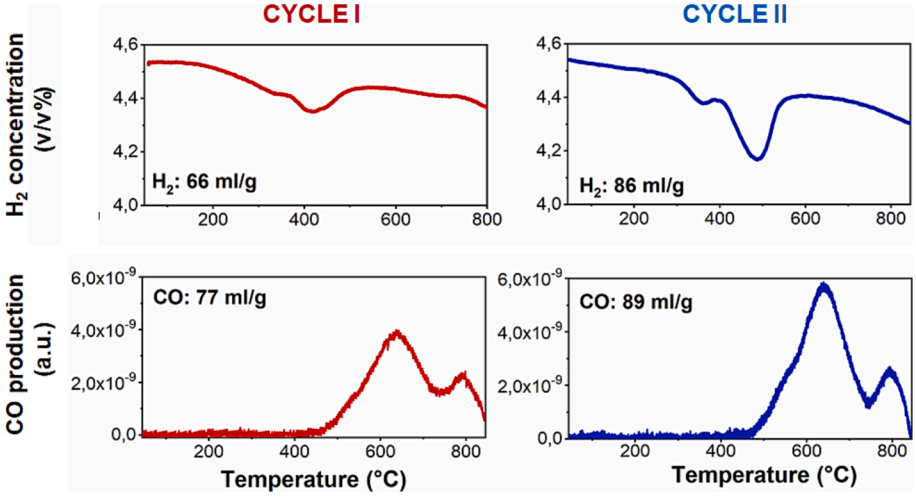

Fig. 7. Results of two RWGS-CL cycles carried out in temperature programmed mode. Reduction profiles in top panels and oxidation profiles in bottom panels. Reduction step: heating ramp at 10 °C/min up to 850 °C followed by an isotherm for 1 h in 5% H_2/N_2 (35 Nml/min). Oxidation step: heating ramp at 10 °C/min up to 850 °C followed by an isotherm for 1 h in 20% CO_2/He (35 Nml/ min).

improvement can be linked to the formation of the Ni-Fe alloy during the exsolution. Recently, density functional theory (DFT) calculations have shown that the Ni_3Fe alloy has the required configuration to adsorb CO_2, thus lowering the activation energy for its reduction [69]. In fact, Ni-doped molybdates have been found to be active and stable electrodes for CO_2 electrolysis, owing to the occurrence of metals exsolution and the formation of specific catalytic sites where the alloy and RP phase work synergically [68,70].

3.3. Long-term stability test

After having identified the optimal temperature for isothermal RWGS-CL cycles based on previous studies, a pristine SFMN sample (40 mg) was tested for 326 RWGS-CL isothermal cycles at 850 °C using a tubular fixed-bed reactor to assess its stability. H_2 and CO_2 were used as reducing and oxidizing gases, respectively, and N_2 as inert gas, with a fixed total volumetric flow rate of 500 Nml/min. The sample powder was initially heated up to the reaction temperature under an inert N_2 atmosphere. After that, the sample was reduced in each cycle under 2.7% H_2/N_2 for 5 min. The reduction reaction was followed by a 3-minute N_2 purging and a 20% CO_2/N_2 oxidation for 5 min under isothermal conditions. The reactor was then purged again with N_2 for 3 min. The results were quantified in terms of CO concentration through online gas analysis. A fast CO production rate peak is observed when CO_2 is sent to the system, before decreasing back to zero after less than 250 s (Fig. 9b). As shown in Fig. 9a, CO specific yield dropped in the first 40 cycles from 2300 μmol/g to values below 1700 μmol/g, then a further slower decrease was observed before stabilization, with a final value above 1500 μmol/g after 250 cycles (≈ 1537 ± 18 μmol/g). This final value is in line with or superior to that measured for other systems as shown in Fig. 10, in which the performance of several iron-based OCs tested in lab-scale reactor configuration have been compared with ceria and ceria-zirconia taken as benchmarks. Fig. 10 reports the CO yield (left axis) along with the number of cycles (right axis) and including the corresponding CO_2 molar concentration applied during the oxidation step of the cycle (percentage value above each bar). It is worth pointing out here that it is not so common to find long time tests for a number of cycles as high as 300+ throughout the literature, as in the present investigation. Most of the works in the literature report a CO production yield after less than 20 redox cycles. The two highest reported yields (4033 μmol/g with $La_{0.75}Sr_{0.25}CoO_3$ [24], and 3500 μmol/g with 50 % LSF/SBA15 [52]) were recorded respectively after 1 cycle and 6 cycles, making it very difficult to assert the better performance over alternative materials in terms of long-duration stability. Moreover, the only case where a higher number of cycles was performed (500 redox cycles with 80 %Fe_2O_3–$Ce_{0.5}Zr_{0.5}O_2$ [13]) shows a long-term CO yield of around 1000 μmol/g, lower that the one reported here for SFMN. Thus, based on this comprehensive literature survey on previous RWGS-CL works, the SFMN yield of 1500 μmol/g reported here is competitive in comparative terms. The results from the long-time test suggest that the transformation of SFMN resulted in a material that showed good performance after stabilization with repeatable yields under the investigated conditions.

After the long-term test, the structure of the sample was characterized by XRD, HAADF-STEM, HRTEM and EDX. The XRD shown in Fig. 11 shows no significant structural changes of the double perovskite, while the metallic phase and small amounts of segregated phases are easily identifiable.

At the nanostructure scale, HAADF-STEM and HRTEM reported in Fig. 12 show evidence of a severe sintering of the matrix with particles up to 500 nm compared to the material shown in Fig. 5. In addition, large well-faceted particles of around 100 nm are clearly visible (see the box in (a), as well as the shell surrounding them showing an enlarged image of (a)). EDX spectra, taken in three different zones of the analyzed area, point out that the particles (green square) are composed of Ni-Fe alloy (very rich in Ni) whereas both the shell (yellow square) and the matrix (orange square) are totally Ni-free and contain Sr, Mo, and Fe ($Sr_2Fe_{1-x}Mo_xO_6$).[1] Sr-Fe-Mo-based double perovskites have been recently investigated as electrodes in SOCs [70,83–86] or as catalysts in the dry reforming of methane [61], showing often exsolution of Ni_xFe alloys and a concomitant partial or complete transformation into RP type layered perovskite phase when reduced in H_2 at high temperature (usually above 800 °C). However, the metal and oxide phases formed after reduction depend on the parent perovskite composition and processing [70,87–88]. To the best of our knowledge, this is the first time that nanoparticles with a core–shell structure are reported for Sr-Fe-Mo-based double perovskites.

The formation of *in-situ* metal/alloy–oxide core–shell-structured nanoparticles during metal or metal alloy exsolution has been recently highlighted by Hou et al. [89] and Tan et al. [90] In this latter study, core–shell structure $NiFe/FeO_x$ (NFA@FeO) nanoparticles have been successfully exsolved from a $Pr_{0.4}Sr_{1.6}(NiFe)_{1.5}Mo_{0.5}O_{6-\delta}$ (PSNFM) double perovskite oxide under controlled reducing conditions. Although the study did not address the mechanism of formation of the core–shell configuration, it demonstrated experimentally and theoretically that in virtu of this peculiar structure, the system NFA@FeO/PSNFM exhibits a much higher rate of CO_2 electrochemical reduction compared to the simple metal/alloy exsolved nanoparticles-decorated perovskites, due to a higher kinetics of CO_2 adsorption, dissociation, and reduction. This was attributed to the formation of the highly defected FeO_x shell, which introduces oxygen vacancies and contributes to extending the active sites from the interface formed between NFA@FeO nanoparticles and PSNFM to the entire surface of NFA@FeO nanoparticles. Probably due to oxygen spillover phenomena, the *in-situ* growth of core–shell nanoparticles generally leads to shells constituted by an oxide of the metal/alloy exsolved [36,40,89–90]. Exsolved NiFe nanoparticle covered with a perovskite oxide as shell was reported by Wu et al. [91] In that study, the prolonged reduction at 800 °C in humidified H_2 of $La_{0.5}Sr_{0.5}Fe_{0.8}Ni_{0.1}Nb_{0.1}O_{3-\delta}$ (LSFNNb0.1) led to the formation of a multifunctional nanoarchitecture (MNA) made by core–shell nanoparticles anchored at a dual-phase oxide substrate. The core–shell nanoparticles were composed of a Ni-Fe alloy core and a RP layered perovskite shell of $SrLaFeO_4$. The formation of this shell stemmed from the decomposition of the parent perovskite, and it was trigged at 800 °C by the co-segregation of B dopants and oxygen vacancies during the exsolution process [34]. The growth of the RP phase proceeded with time until the formation of an encapsulating layer able to contrast the sintering of exsolved metal alloy nanoparticles and the further decomposition of parent perovskite. The rate of formation of the MNA, consisting of RP/Fe-Ni alloy core–shell nanoparticles embedded in a substrate with RP/SP heterostructures, was related to the thermodynamic stability of parent perovskite and the kinetics of RP formation in the selected reducing conditions, thus depending on the type of atmosphere and temperature. The formation mechanism of such a composite catalyst may resemble the one leading to the core–shell structure in our study. XRD and HRTEM results showed that prolonged reduction at high temperature caused the exsolution of Ni-Fe particles along with the formation of perovskite-like phases, in particular an RP phase with formula $Sr_3MoFeO_{7-\delta}$, which works synergically as catalyst to promote the activation and reduction of CO_2 as demonstrated by TPR-TPO cycles. HRTEM results (Fig. 5) are compatible with the formation of a core–shell structure during the first redox cycles. As the exsolution proceeds, we assisted the sintering of nanoparticles in well faceted nanoparticles, and the segregation of strontium-based phases, which can explain the

[1] *The experimental results are highly compatible with a core–shell structure. Due to the nature of the sample, which is highly sintered, a more powerful microscope would be necessary to obtain additional microstructural data. Unfortunately we do not have access to this instrumentation at present. Further advanced characterizations devoted to understanding in depth the structural changes of the SFMN during cycles are planned for future studies.*

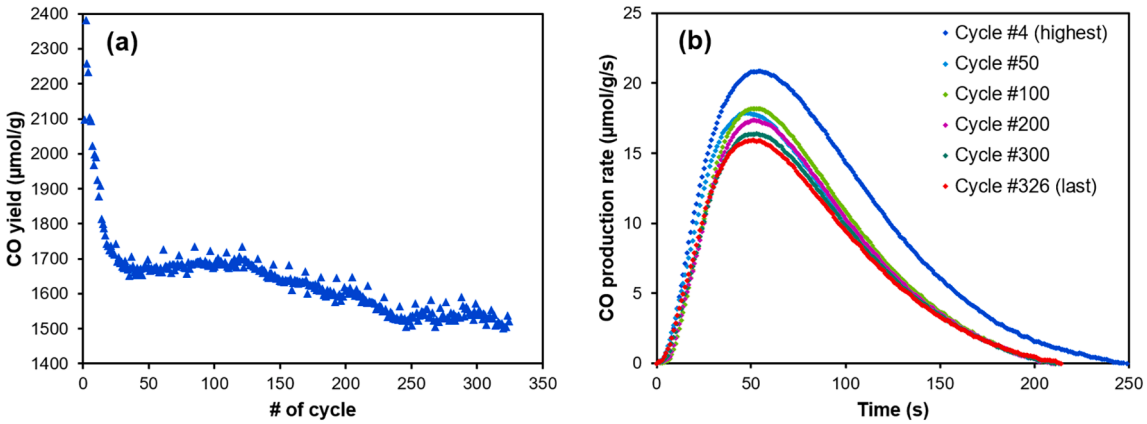

Fig. 9. Isothermal (850 °C) stability test of 320 + cycles on SFMN with 40 mg sample mass. Total flow rate of 500 Nml/min – Reduction in 2.7% H_2/N_2 for 5 min – Oxidation in 20% CO_2/N_2 for 5 min – Purging in N_2 in between for 3 min. (a) CO specific yield stabilization over the entire test. Values are referred to the initial oxidized mass. (b) Selected CO production rate peaks.

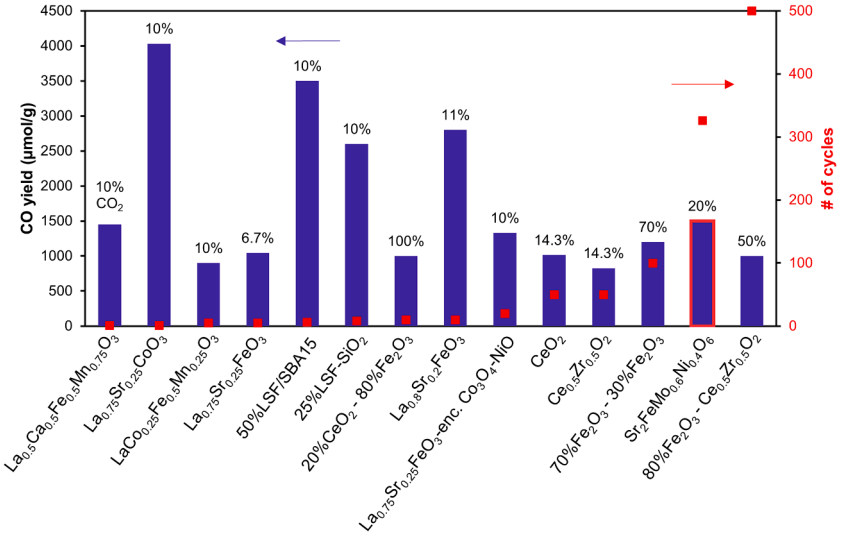

Fig. 10. *Selected studies on RWGS-CL from literature along with the present work (red-contoured bar). OCs are compared in terms of CO yield (left axis) for increasing cycle number (right axis) to which the reported yield is referred. The percentage on the bars shows the applied CO_2 molar concentration during the test. The reference works, in the order from left to right, are the following: $La_{0.5}Ca_{0.5}Fe_{0.25}Mn_{0.75}O_3$ [26] – $La_{0.75}Sr_{0.25}CoO_3$ [24] – $LaCo_{0.25}Fe_{0.50}Mn_{0.25}O_3$ [78] – $La_{0.75}Sr_{0.25}FeO_3$ [33] – 50 %LSF/SBA-15* [52] *– 25 %LSF-SiO_2* [79] *– 20 %CeO_2-80 %Fe_2O_3* [80] *– $La_{0.8}Sr_{0.2}FeO_3$* [81] *(yield is referred to the total redox catalyst mass) – $La_{0.75}Sr_{0.25}FeO_3$-encapsulated Co_3O_4-NiO* [49] *– CeO_2* [18] *– $Ce_{0.5}Zr_{0.5}O_2$* [18] *– 70% Fe_2O_3-30% Al_2O_3* [82]*(yield is referred to the Fe_2O_3 mass in the mixed oxide sample) – $Sr_2FeMo_{0.6}Ni_{0.4}O_6$ (this work) – 80% Fe_2O_3-$Ce_{0.5}Zr_{0.5}O_2$* [13]. (For interpretation of the references to colour in this figure legend, the reader is referred to the web version of this article.)

deactivation observed in the first 50 redox cycles. In addition, we observed the thickening of the shell layer. The growth and shape of exsolved nanoparticles has been proven to be dependent on the reduction conditions [92]. For instance, Neagu et al. [93] observed the formation of faceted rather than round Ni nanoparticles when the exsolution process was carried in argon. It is therefore inferred that the redox cycling conditions play a crucial role in defining the final nanostructure of the OC derived from $Sr_2FeMo_{0.6}Ni_{0.4}O_6$ transformation.

The exsolution of Ni and Fe from the B sites leads to the formation of stable perovskite phases under reducing conditions that may undergo partial decomposition when switching to oxidising conditions [92]. The presence of $SrCO_3$ and $SrMoO_4$ impurities after cycling confirms an evolution of the initial composition. Therefore, during the cycles, , as proposed by Wu et al. [91], a rearrangement of the oxide phases formed by the transformation can be espected to occur to obtain a configuration of phases and interfaces in which the core–shell structure helps to stabilise the metal nanoparticles. The growth of embedded Ni-Fe particles with the adoption of a polyhedral shape, which generally has larger surface and interface in comparison to spherical particles with the same volume, needs the adhesion between Ni and support to be strong enough to overcome the increase of surface and interface area due to the shape-shifting [81]. It is likely that the development of the core–shell structure is driven by the necessity of enhancing the adhesion of Ni-Fe particles as they grow; however, further studies are required to assess the driving forces that rule the formation of a core–shell structure during the CL process. On the other hand, the perovskite shell introduces additional sites for CO_2 activation [49,90], which can compensate for the loss of active sites due to the sintering of metal particles. Moreover, as proposed by Tan et al. [90], such a configuration could favour oxygen exchange with the perovskites substrate, in turn characterised by RP/perovskite interfaces with fast oxygen exchange kinetics [94–95].

To sum up the results of this work, during redox H_2/CO_2 cycles the double perovskite $Sr_2FeMo_{0.6}Ni_{0.4}O_6$ is transformed into a multiphase and multifunctional system which shows good and stable oxygen exchange capacity for the RWGS-CL process, and can effectively operate under isothermal conditions in the temperature range 750–850 °C. The phases formed from the exsolution work synergistically: the exsolved NiFe nanoparticles promote the adsorption and activation of the

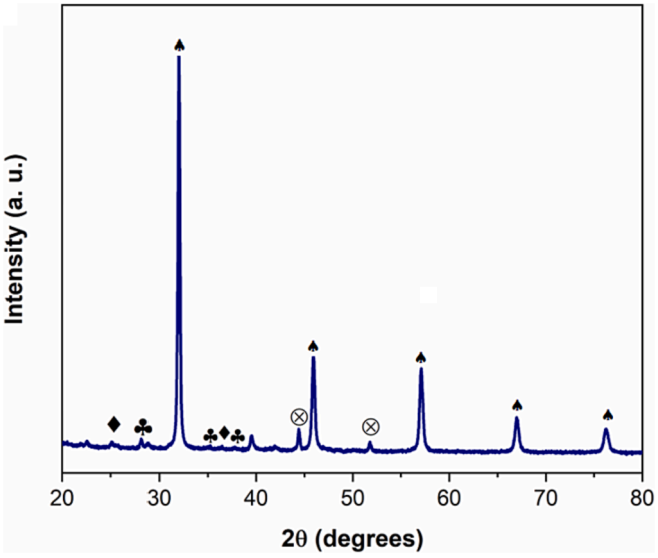

Fig. 11. *XRD of the SFMN sample long-tested with 326 isothermal cycles at 850 °C. Total flow rate of 500 Nml/min – Cycle: Reduction in 2.7% H_2/N_2 for 5 min – Oxidation in 20% CO_2/N_2 for 5 min – Purging in N_2 in between for 3 min. $SrCO_3$ (◆), $SrMoO_4$ (♣), Sr_2FeMoO_6 (♠), Ni-Fe (⊗).*

reactants (H_2 and CO_2) and the RP phase facilitates the oxygen exchange kinetics in the two steps of the cycle. Moreover, the self-assembly of the active phases in a core–shell configuration contributes to strengthening this synergism by extending the catalytic surface for the adsorption and activation of CO_2 not only to the NiFe/RP interface, but to the entire surface of the nanoparticles. This would counterbalance the activity losses due to sintering of NiFe nanoparticles with the redox cycles.

4. Conclusions and perspectives

In this work, we investigate for the first time the double perovskite $Sr_2FeMo_{0.6}Ni_{0.4}O_6$ as oxygen carrier (OC) for RWGS-CL cycles. We observe the promotion of both reduction and oxidation steps being correlated with the exsolution of Ni-Fe alloy and the formation of the RP phase $Sr_3FeMoO_{7-\delta}$. These latter processes require temperature above 800 °C to be fully completed. The multi-phase perovskite-like OC formed after reduction shows high performance and high stability in comparison to many perovskites and materials tested in the literature for the same application, with optimal operating conditions at 750–850 °C in isothermal cycles. The enhanced performance of this material is due to the cooperative action between the phases formed: the NiFe alloy nanoparticles promote the adsorption and the activation of reactants (H_2 and CO_2) and the RP-phase facilitates the fast exchange of oxygen in the two steps of the cycle. We observe that the CO_2 oxidizing atmosphere is responsible for segregation phenomena, which are luckily reversible under the investigated operating conditions. In addition, redox cycling conditions promote the formation of a core–shell structure, consisting of a Ni-Fe alloy as the core and a perovskites-derived shell as demonstrated by HAADF-STM and HRTEM characterizations. This rearrangement helps to create new sites of CO_2 adsorption and may play a role in counteracting the effect of the sintering processes. Its significance in the CL process will have to be further investigated.

This study paves the way for the engineering of new OCs based on metal-doped $Sr_2Fe_{1-x}Mo_xO_6$ double perovskites by the exsolution of their dopants. This approach will require further studies on both the composition and optimal level of dopants, as well as on procedure for accelerating the exsolution and the phase transformation at lower temperatures.

Declaration of Competing Interest

The authors declare that they have no known competing financial interests or personal relationships that could have appeared to influence the work reported in this paper.

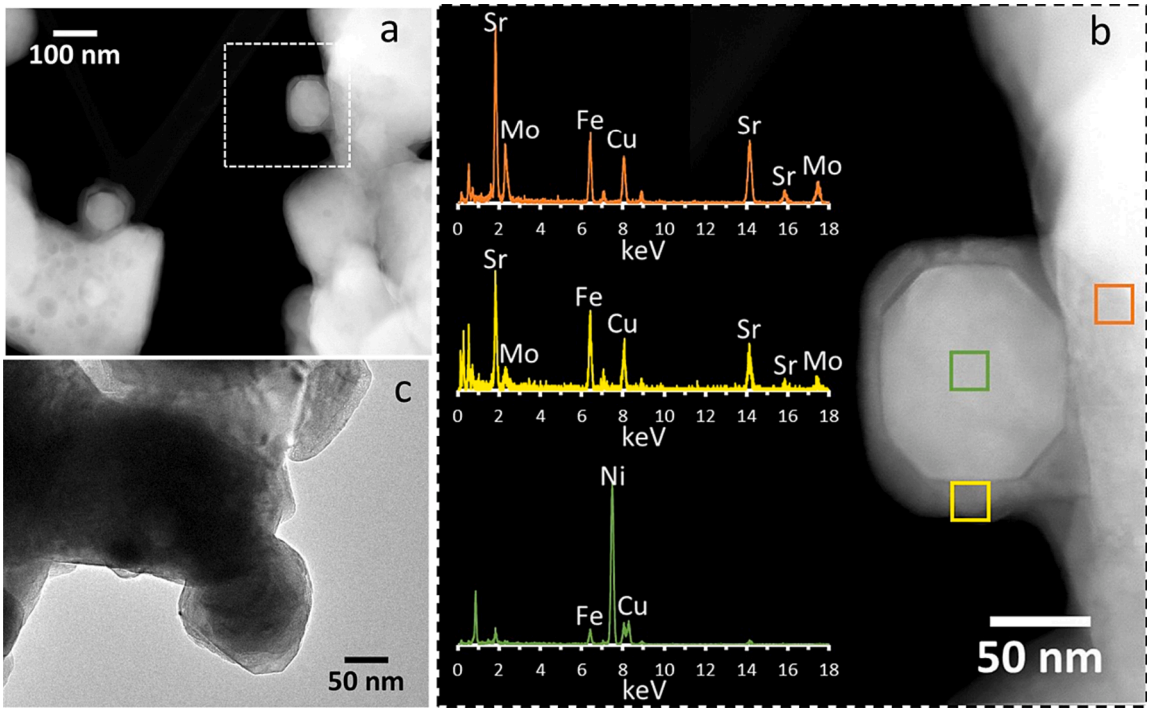

Fig. 12. HAADF-STEM images of the sample tested for hundreds of H_2/CO_2-redox cycles at 850 °C (a) low magnification. (b) Square area in (a) but at high magnification along with EDX analysis done at the three squares in the same image shown at the corresponding colors. (c) HRTEM image.

Data availability

Data will be made available on request.

Acknowledgments

J.L. is a Serra Húnter Fellow and is grateful to the ICREA Academia program and projects MICINN/FEDER PID2021-124572OB-C31 and GC 2021 SGR 01061. The "MIT-FVG-SISSA" (year 2019) project has been funded within MIT International Science and Technology Initiatives (MISTI) by Region Friuli Venezia Giulia (FVG) and the Massachusetts Institute of Technology (MIT). A.F. thanks MIUR for funds, PRIN project-DIRECTBIOSOFC, 2017FCFYHK, 2019–2022.

Appendix A. Supplementary data

Supplementary data to this article can be found online at https://doi.org/10.1016/j.cej.2023.146083.

References

[1] IEA (2023). *CO2 Emissions in 2022*; International Energy Agency: Paris, 2023. https://www.iea.org/reports/co2-emissions-in-2022 (accessed 2023-04-21).
[2] O. Edenhofer, Climate Change 2014: Mitigation of Climate Change, Cambridge University Press, 2015. Assessment report.
[3] N. Siefert, S. Narburgh, Y. Chen, Comprehensive Exergy Analysis of Three IGCC Power Plant Configurations with CO2 Capture, Energies 9 (9) (2016) 669, https://doi.org/10.3390/en9090669.
[4] *The Role of CCUS in Low-Carbon Power Systems*; Paris, 2020.
[5] R. Chauvy, G. De Weireld, CO 2 Utilization Technologies in Europe: A Short Review, Energ. Technol. 8 (12) (2020) 2000627, https://doi.org/10.1002/ente.202000627.
[6] M. Romero, A. Steinfeld, Concentrating Solar Thermal Power and Thermochemical Fuels, Energ. Environ. Sci. 5 (11) (2012) 9234–9245.
[7] Farooqui, A.; Boaro, M.; Llorca, J.; Santarelli, M. Solar Fuels via Two-Step Thermochemical Redox Cycles. In *Advances in Greener Energy Technologies*; Bhoi, A. K., Sherpa, K. S., Kalam, A., Chae, G.-S., Eds.; Springer Singapore: Singapore, 2020; pp 31–84. https://doi.org/10.1007/978-981-15-4246-6_3.
[8] W.J. Lee, C. Li, H. Prajitno, J. Yoo, J. Patel, Y. Yang, S. Lim, Recent Trend in Thermal Catalytic Low Temperature CO2 Methanation: A Critical Review, Catal. Today 368 (2021) 2–19.
[9] M. González-Castaño, B. Dorneanu, H. Arellano-García, The Reverse Water Gas Shift Reaction: A Process Systems Engineering Perspective, React. Chem. Eng. 6 (6) (2021) 954–976.
[10] S. Xu, E.A. Carter, Theoretical Insights into Heterogeneous (Photo) Electrochemical CO2 Reduction, Chem. Rev. 119 (11) (2018) 6631–6669.
[11] S. Nitopi, E. Bertheussen, S.B. Scott, X. Liu, A.K. Engstfeld, S. Horch, B. Seger, I. E. Stephens, K. Chan, C. Hahn, et al., Progress and Perspectives of Electrochemical CO2 Reduction on Copper in Aqueous Electrolyte, Chem. Rev. 119 (12) (2019) 7610–7672.
[12] G.H. Han, J. Bang, G. Park, S. Choe, Y.J. Jang, H.W. Jang, S.Y. Kim, S.H. Ahn, Recent Advances in Electrochemical, Photochemical, and Photoelectrochemical Reduction of CO2 to C2+ Products, Small 2205765 (2023).
[13] M. Wenzel, N.A. Dharanipragada, V.V. Galvita, H. Poelman, G.B. Marin, L. Rihko-Struckmann, K. Sundmacher, CO Production from CO2 via Reverse Water-Gas Shift Reaction Performed in a Chemical Looping Mode: Kinetics on Modified Iron Oxide, J. CO2 Util. 17 (2017) 60–68.
[14] L. Zeng, Z. Cheng, J.A. Fan, L.-S. Fan, J. Gong, Metal Oxide Redox Chemistry for Chemical Looping Processes, Nat. Rev. Chem. 2 (11) (2018) 349–364.
[15] J.R. Scheffe, A. Steinfeld, Oxygen Exchange Materials for Solar Thermochemical Splitting of H2O and CO2: A Review, Mater. Today 17 (7) (2014) 341–348.
[16] J. Hu, V.V. Galvita, H. Poelman, G.B. Marin, Advanced Chemical Looping Materials for CO2 Utilization: A Review, Materials 11 (7) (2018) 1187.
[17] R.R. Bhosale, G. Takalkar, P. Sutar, A. Kumar, F. AlMomani, M. Khraisheh, A Decade of Ceria Based Solar Thermochemical H2O/CO2 Splitting Cycle, Int. J. Hydrogen Energy 44 (1) (2019) 34–60.
[18] Z. Zhao, M. Uddi, N. Tsvetkov, B. Yildiz, A.F. Ghoniem, Enhanced Intermediate-Temperature CO 2 Splitting Using Nonstoichiometric Ceria and Ceria-Zirconia, PCCP 19 (37) (2017) 25774–25785.
[19] S. Ackermann, L. Sauvin, R. Castiglioni, J.L. Rupp, J.R. Scheffe, A. Steinfeld, Kinetics of CO2 Reduction over Nonstoichiometric Ceria, J. Phys. Chem. C 119 (29) (2015) 16452–16461.
[20] A. Farooqui, A.M. Pica, P. Marocco, D. Ferrero, A. Lanzini, S. Fiorilli, J. Llorca, M. Santarelli, Assessment of Kinetic Model for Ceria Oxidation for Chemical-Looping CO2 Dissociation, Chem. Eng. J. 346 (2018) 171–181.
[21] D. Maiti, B.J. Hare, Y.A. Daza, A.E. Ramos, J.N. Kuhn, V.R. Bhethanabotla, Earth Abundant Perovskite Oxides for Low Temperature CO 2 Conversion, Energ. Environ. Sci. 11 (3) (2018) 648–659.
[22] A. Bayon, A. de la Calle, K.K. Ghose, A. Page, R. McNaughton, Experimental, Computational and Thermodynamic Studies in Perovskites Metal Oxides for Thermochemical Fuel Production: A Review, Int. J. Hydrogen Energy 45 (23) (2020) 12653–12679.
[23] M. Wenzel, L. Rihko-Struckmann, K. Sundmacher, Thermodynamic Analysis and Optimization of RWGS Processes for Solar Syngas Production from CO2, AIChE J 63 (1) (2017) 15–22.
[24] Y.A. Daza, R.A. Kent, M.M. Yung, J.N. Kuhn, Carbon Dioxide Conversion by Reverse Water-Gas Shift Chemical Looping on Perovskite-Type Oxides, Ind. Eng. Chem. Res. 53 (14) (2014) 5828–5837.
[25] L. Zhang, L. Mei, K. Wang, Y. Lv, S. Zhang, Y. Lian, X. Liu, Z. Ma, G. Xiao, Q. Liu, S. Zhai, S. Zhang, G. Liu, L. Yuan, B. Guo, Z. Chen, K. Wei, A. Liu, S. Yue, G. Niu, X. Pan, J. Sun, Y. Hua, W.-Q. Wu, D. Di, B. Zhao, J. Tian, Z. Wang, Y. Yang, L. Chu, M. Yuan, H. Zeng, H.-L. Yip, K. Yan, W. Xu, L. Zhu, W. Zhang, G. Xing, F. Gao, L. Ding, Advances in the Application of Perovskite Materials, Nano-Micro Lett. 15 (1) (2023) 177, https://doi.org/10.1007/s40820-023-01140-3.
[26] B.J. Hare, D. Maiti, A.J. Meier, V.R. Bhethanabotla, J.N. Kuhn, CO2 Conversion Performance of Perovskite Oxides Designed with Abundant Metals, Ind. Eng. Chem. Res. 58 (28) (2019) 12551–12560.
[27] E. Marek, W. Hu, M. Gaultois, C.P. Grey, S.A. Scott, The Use of Strontium Ferrite in Chemical Looping Systems, Appl. Energy 223 (2018) 369–382.
[28] M. Pena, J. Fierro, Chemical Structures and Performance of Perovskite Oxides, Chem. Rev. 101 (7) (2001) 1981–2018.
[29] J. Wu, R. Ye, D.-J. Xu, L. Wan, T.R. Reina, H. Sun, Y. Ni, Z.-F. Zhou, X. Deng, Emerging Natural and Tailored Perovskite-Type Mixed Oxides-Based Catalysts for CO2 Conversions. Frontiers, Chemistry (2022) 10.
[30] C. Sun, J.A. Alonso, J. Bian, Recent Advances in Perovskite-Type Oxides for Energy Conversion and Storage Applications, Adv. Energy Mater. 11 (2) (2021) 2000459, https://doi.org/10.1002/aenm.202000459.
[31] X. Xu, W. Wang, W. Zhou, Z. Shao, Recent Advances in Novel Nanostructuring Methods of Perovskite Electrocatalysts for Energy-Related Applications, Small Methods 2 (7) (2018) 1800071, https://doi.org/10.1002/smtd.201800071.
[32] X. Li, H. Zhao, J. Liang, Y. Luo, G. Chen, X. Shi, S. Lu, S. Gao, J. Hu, Q. Liu, et al., A-Site Perovskite Oxides: An Emerging Functional Material for Electrocatalysis and Photocatalysis, J. Mater. Chem. A 9 (11) (2021) 6650–6670.
[33] Daza, Y. A.; Maiti, D.; Kent, R. A.; Bhethanabotla, V. R.; Kuhn, J. N. Isothermal Reverse Water Gas Shift Chemical Looping on La0. 75Sr0. 25Co (1- Y) FeYO3 Perovskite-Type Oxides. *Catalysis Today* **2015**, *258*, 691–698.
[34] O. Kwon, S. Sengodan, K. Kim, G. Kim, H.Y. Jeong, J. Shin, Y.-W. Ju, J.W. Han, G. Kim, Exsolution Trends and Co-Segregation Aspects of Self-Grown Catalyst Nanoparticles in Perovskites, Nat. Commun. 8 (1) (2017) 15967.
[35] O. Kwon, S. Joo, S. Choi, S. Sengodan, G. Kim, Review on Exsolution and Its Driving Forces in Perovskites, Journal of Physics: Energy 2 (3) (2020), 032001.
[36] C. Tang, K. Kousi, D. Neagu, I.S. Metcalfe, Trends and Prospects of Bimetallic Exsolution. *Chemistry–A*, European Journal 27 (22) (2021) 6666–6675.
[37] Q. Yang, G. Liu, Y. Liu, Perovskite-Type Oxides as the Catalyst Precursors for Preparing Supported Metallic Nanocatalysts: A Review, Ind. Eng. Chem. Res. 57 (1) (2018) 1–17.
[38] D. Neagu, J.T.S. Irvine, J. Wang, B. Yildiz, A.K. Opitz, J. Fleig, Y. Wang, J. Liu, L. Shen, F. Ciucci, B.A. Rosen, Y. Xiao, K. Xie, G. Yang, Z. Shao, Y. Zhang, J. M. Reinke, T.A. Schmauss, S. Barnett, R. Maring, V. Kyriakou, U. Mushtaq, M. N. Tsampas, Y. Kim, R. O'Hayre, A.J. Carrillo, T. Ruh, L. Lindenthal, F. Schrenk, C. Rameshan, E.I. Papaioannou, K. Kousi, I. Metcalfe, X. Xu, G. Liu, Roadmap on Exsolution for Energy Applications, J. Phys. Energy (2023), https://doi.org/10.1088/2515-7655/acd146.
[39] T. Cao, O. Kwon, R.J. Gorte, J.M. Vohs, Metal Exsolution to Enhance the Catalytic Activity of Electrodes in Solid Oxide Fuel Cells, Nanomaterials 10 (12) (2020) 2445, https://doi.org/10.3390/nano10122445.
[40] K. Kousi, C. Tang, I.S. Metcalfe, D. Neagu, Emergence and Future of Exsolved Materials, Small 17 (21) (2021) 2006479.
[41] L. Lindenthal, J. Popovic, R. Rameshan, J. Huber, F. Schrenk, T. Ruh, A. Nenning, S. Löffler, A.K. Opitz, C. Rameshan, Novel Perovskite Catalysts for CO2 Utilization - Exsolution Enhanced Reverse Water-Gas Shift Activity, Appl Catal B 292 (2021), 120183, https://doi.org/10.1016/j.apcatb.2021.120183.
[42] G. Dimitrakopoulos, A.F. Ghoniem, B. Yildiz, In Situ Catalyst Exsolution on Perovskite Oxides for the Production of CO and Synthesis Gas in Ceramic Membrane Reactors, Sustainable Energy Fuels 3 (9) (2019) 2347–2355, https://doi.org/10.1039/C9SE00249A.
[43] S.-K. Otto, K. Kousi, D. Neagu, L. Bekris, J. Janek, I.S. Metcalfe, Exsolved Nickel Nanoparticles Acting as Oxygen Storage Reservoirs and Active Sites for Redox CH4 Conversion, ACS Appl. Energy Mater. 2 (10) (2019) 7288–7298, https://doi.org/10.1021/acsaem.9b01267.
[44] K. Kousi, D. Neagu, L. Bekris, E.I. Papaioannou, I.S. Metcalfe, Endogenous Nanoparticles Strain Perovskite Host Lattice Providing Oxygen Capacity and Driving Oxygen Exchange and CH4 Conversion to Syngas, Angew. Chem. Int. Ed. 59 (6) (2020) 2510–2519, https://doi.org/10.1002/anie.201915140.
[45] K. Kousi, D. Neagu, L. Bekris, E. Calì, G. Kerherve, E.I. Papaioannou, D.J. Payne, I. S. Metcalfe, Low Temperature Methane Conversion with Perovskite-Supported Exo/Endo-Particles, J. Mater. Chem. A 8 (25) (2020) 12406–12417, https://doi.org/10.1039/D0TA05122E.
[46] A.J. Carrillo, K.J. Kim, Z.D. Hood, A.H. Bork, J.L.M. Rupp, La0.6Sr0.4Cr0.8Co0.2O3 Perovskite Decorated with Exsolved Co Nanoparticles for Stable CO2 Splitting and Syngas Production, ACS Appl. Energy Mater. 3 (5) (2020) 4569–4579, https://doi.org/10.1021/acsaem.0c00249.
[47] D. Hosseini, F. Donat, P.M. Abdala, S.M. Kim, A.M. Kierzkowska, C.R. Müller, Reversible Exsolution of Dopant Improves the Performance of Ca2Fe2O5 for Chemical Looping Hydrogen Production, ACS Appl. Mater. Interfaces 11 (20) (2019) 18276–18284, https://doi.org/10.1021/acsami.8b16732.

[48] H.S. Lim, Y. Kim, D. Kang, M. Lee, A. Jo, J.W. Lee, Fundamental Aspects of Enhancing Low-Temperature CO2 Splitting to CO on a Double La2NiFeO6 Perovskite, ACS Catal. 11 (19) (2021) 12220–12231.

[49] M. Lee, Y. Kim, H.S. Lim, A. Jo, D. Kang, J.W. Lee, Reverse Water-Gas Shift Chemical Looping Using a Core-Shell Structured Perovskite Oxygen Carrier, Energies 13 (20) (2020) 5324.

[50] K. Efimov, O. Czuprat, A. Feldhoff, In-Situ X-Ray Diffraction Study of Carbonate Formation and Decomposition in Perovskite-Type BCFZ, J. Solid State Chem. 184 (5) (2011) 1085–1089.

[51] B.J. Hare, D. Maiti, S. Ramani, A.E. Ramos, V.R. Bhethanabotla, J.N. Kuhn, Thermochemical Conversion of Carbon Dioxide by Reverse Water-Gas Shift Chemical Looping Using Supported Perovskite Oxides, Catal. Today 323 (2019) 225–232.

[52] J.C. Brower, B.J. Hare, V.R. Bhethanabotla, J.N. Kuhn, Mesoporous Silica Supported Perovskite Oxides for Low Temperature Thermochemical CO2 Conversion, ChemCatChem 12 (24) (2020) 6317–6328.

[53] D. Zeng, Y. Qiu, L. Ma, M. Li, D. Cui, S. Zhang, R. Xiao, Tuning the Support Properties toward Higher CO2 Conversion during a Chemical Looping Scheme, Environ. Sci. Tech. 54 (19) (2020) 12467–12475.

[54] X. Xu, Y. Zhong, Z. Shao, Double Perovskites in Catalysis, Electrocatalysis, and Photo(Electro)Catalysis, Trends in Chemistry 1 (4) (2019) 410–424, https://doi.org/10.1016/j.trechm.2019.05.006.

[55] X. Xu, Y. Pan, Y. Zhong, R. Ran, Z. Shao, Ruddlesden-Popper Perovskites in Electrocatalysis, Mater. Horiz. 7 (10) (2020) 2519–2565, https://doi.org/10.1039/D0MH00477D.

[56] L. Skutina, E. Filonova, D. Medvedev, A. Maignan, Undoped Sr2MMoO6 Double Perovskite Molybdates (M = Ni, Mg, Fe) as Promising Anode Materials for Solid Oxide Fuel Cells, Materials 14 (7) (2021) 1715, https://doi.org/10.3390/ma14071715.

[57] Y.-H. Huang, G. Liang, M. Croft, M. Lehtimäki, M. Karppinen, J.B. Goodenough, Double-Perovskite Anode Materials Sr 2 MMoO 6 (M = Co, Ni) for Solid Oxide Fuel Cells, Chem. Mater. 21 (11) (2009) 2319–2326, https://doi.org/10.1021/cm8033643.

[58] Y. Jiang, Y. Yang, C. Xia, H.J.M. Bouwmeester, Sr 2 Fe 1.4 Mn 0.1 Mo 0.5 O 6−δ Perovskite Cathode for Highly Efficient CO 2 Electrolysis, J. Mater. Chem. A 7 (40) (2019) 22939–22949, https://doi.org/10.1039/C9TA07689A.

[59] N. Dai, J. Feng, Z. Wang, T. Jiang, W. Sun, J. Qiao, K. Sun, Synthesis and Characterization of B-Site Ni-Doped Perovskites Sr2Fe1.5−xNixMo0.5O6−δ (x = 0, 0.05, 0.1, 0.2, 0.4) as Cathodes for SOFCs, J. Mater. Chem. A 1 (45) (2013) 14147, https://doi.org/10.1039/c3ta13607h.

[60] Z. Xie, H. Zhao, Z. Du, T. Chen, N. Chen, Electrical, Chemical, and Electrochemical Properties of Double Perovskite Oxides Sr 2 Mg 1–x Ni x MoO 6−δ as Anode Materials for Solid Oxide Fuel Cells, J. Phys. Chem. C 118 (33) (2014) 18853–18860, https://doi.org/10.1021/jp502503e.

[61] A.J. Carrillo, J.M. Serra, Exploring the Stability of Fe–Ni Alloy Nanoparticles Exsolved from Double-Layered Perovskites for Dry Reforming of Methane, Catalysts 11 (6) (2021) 741.

[62] C. Li, W. Wang, C. Xu, Y. Liu, B. He, C. Chen, Double Perovskite Oxides Sr2Mg1-XFexMoO6-δ for Catalytic Oxidation of Methane, J. Nat. Gas Chem. 20 (4) (2011) 345–349.

[63] G. Xiao, Q. Liu, S. Wang, V.G. Komvokis, M.D. Amiridis, A. Heyden, S. Ma, F. Chen, Synthesis and Characterization of Mo-Doped SrFeO3−δ as Cathode Materials for Solid Oxide Fuel Cells, J. Power Sources 202 (2012) 63–69, https://doi.org/10.1016/j.jpowsour.2011.11.021.

[64] J. Rager, M. Zipperle, A. Sharma, J.L. MacManus-Driscoll, Oxygen Stoichiometry in Sr2FeMoO6, the Determination of Fe and Mo Valence States, and the Chemical Phase Diagram of SrO-Fe3O4-MoO3, J. Am. Ceram. Soc. 87 (7) (2004) 1330–1335, https://doi.org/10.1111/j.1151-2916.2004.tb07730.x.

[65] Y. Song, Q. Zhong, W. Tan, C. Pan, Effect of Cobalt-Substitution Sr2Fe1.5-XCoxMo0.5O6-δ for Intermediate Temperature Symmetrical Solid Oxide Fuel Cells Fed with H2–H2S, Electrochim. Acta 139 (2014) 13–20, https://doi.org/10.1016/j.electacta.2014.07.022.

[66] J. Feng, G. Yang, N. Dai, Z. Wang, W. Sun, D. Rooney, J. Qiao, K. Sun, Investigation into the Effect of Fe-Site Substitution on the Performance of Sr 2 Fe 1.5 Mo 0.5 O 6−δ Anodes for SOFCs, J. Mater. Chem. A 2 (41) (2014) 17628–17634, https://doi.org/10.1039/C4TA03216K.

[67] Z. Du, H. Zhao, S. Yi, Q. Xia, Y. Gong, Y. Zhang, X. Cheng, Y. Li, L. Gu, K. Świerczek, High-Performance Anode Material Sr 2 FeMo 0.65 Ni 0.35 O 6−δ with In Situ Exsolved Nanoparticle Catalyst, ACS Nano 10 (9) (2016) 8660–8669, https://doi.org/10.1021/acsnano.6b03979.

[68] Y. Li, M. Singh, Z. Zhuang, Y. Jing, F. Li, K. Maliutina, C. He, L. Fan, Efficient Reversible CO/CO2 Conversion in Solid Oxide Cells with a Phase-Transformed Fuel Electrode, Sci. China Mater. 64 (5) (2021) 1114–1126, https://doi.org/10.1007/s40843-020-1531-7.

[69] Y. Li, Y. Li, S. Zhang, C. Ren, Y. Jing, F. Cheng, Q. Wu, P. Lund, L. Fan, Mutual Conversion of CO–CO 2 on a Perovskite Fuel Electrode with Endogenous Alloy Nanoparticles for Reversible Solid Oxide Cells, ACS Appl. Mater. Interfaces 14 (7) (2022) 9138–9150, https://doi.org/10.1021/acsami.1c23548.

[70] H. Lv, L. Lin, X. Zhang, D. Gao, Y. Song, Y. Zhou, Q. Liu, G. Wang, Bao X. In Situ Exsolved FeNi 3 Nanoparticles on Nickel Doped Sr 2 Fe 1.5 Mo 0.5 O 6−δ Perovskite for Efficient Electrochemical CO 2 Reduction Reaction, J. Mater. Chem. A 7 (19) (2019) 11967–11975, https://doi.org/10.1039/C9TA5D.

[71] Q. Liu, X. Dong, G. Xiao, F. Zhao, F. Chen, A Novel Electrode Material for Symmetrical SOFCs, Adv. Mater. 22 (48) (2010) 5478–5482.

[72] M. Cernea, F. Vasiliu, C. Bartha, C. Plapcianu, I. Mercioniu, Characterization of Ferromagnetic Double Perovskite Sr2FeMoO6 Prepared by Various Methods, Ceram. Int. 40 (8) (2014) 11601–11609.

[73] A. Jain, S. Ong, G. Hautier, W. Chen, W. Richards, S. Dacek, S. Cholia, D. Gunter, D. Skinner, G. Ceder, others, A Materials Genome Approach to Accelerating Materials Innovation, APL Mater, The Materials Project, 2013.

[74] Z. Singh, R. Prasad, S. Dash, D. Sood, Determination of Standard Molar Gibbs' Energy of Formation of Sr3MoO6 (s), J. Alloy. Compd. 209 (1–2) (1994) 193–196.

[75] K.H. Stern, High Temperature Properties and Thermal Decomposition of Inorganic Salts with Oxyanions, CRC Press, 2000.

[76] L. Duranti, A. Felli, M. Marelli, M. Dosa, E.D. Bartolomeo, M. Piumetti, M. Boaro, Study on Exsolution Process of Sr2FeMo0.6Ni0.4O6 via in Situ Cathodic Polarization, ECS Trans. 111 (6) (2023) 609, https://doi.org/10.1149/11106.0609ecst.

[77] H. Li, Y. Song, M. Xu, W. Wang, R. Ran, W. Zhou, Z. Shao, Exsolved Alloy Nanoparticles Decorated Ruddlesden-Popper Perovskite as Sulfur-Tolerant Anodes for Solid Oxide Fuel Cells, Energy Fuel 34 (9) (2020) 11449–11457.

[78] A.E. Ramos, D. Maiti, Y.A. Daza, J.N. Kuhn, V.R. Bhethanabotla, Co, Fe, and Mn in La-Perovskite Oxides for Low Temperature Thermochemical CO2 Conversion, Catal. Today 338 (2019) 52–59.

[79] B.J. Hare, D. Maiti, Y.A. Daza, V.R. Bhethanabotla, J.N. Kuhn, Enhanced CO2 Conversion to CO by Silica-Supported Perovskite Oxides at Low Temperatures, ACS Catal. 8 (4) (2018) 3021–3029.

[80] V.V. Galvita, H. Poelman, V. Bliznuk, C. Detavernier, G.B. Marin, CeO2-Modified Fe2O3 for CO2 Utilization via Chemical Looping, Ind. Eng. Chem. Res. 52 (25) (2013) 8416–8426.

[81] A. Jo, Y. Kim, H.S. Lim, M. Lee, D. Kang, J.W. Lee, Controlled Template Removal from Nanocast La0. 8Sr0. 2FeO3 for Enhanced CO2 Conversion by Reverse Water Gas Shift Chemical Looping, J. CO2 Util. 56 (2022), 101845.

[82] L.K. Rihko-Struckmann, P. Datta, M. Wenzel, K. Sundmacher, N.V.R. A. Dharanipragada, H. Poelman, V.V. Galvita, G.B. Marin, Hydrogen and Carbon Monoxide Production by Chemical Looping over Iron-Aluminium Oxides, Energ. Technol. 4 (2) (2016) 304–313.

[83] Y. Wang, T. Liu, M. Li, C. Xia, B. Zhou, F. Chen, Exsolved Fe–Ni Nano-Particles from Sr2Fe1.3Ni0.2Mo0.5O6 Perovskite Oxide as a Cathode for Solid Oxide Steam Electrolysis Cells, J. Mater. Chem. A 4 (37) (2016) 14163–14169, https://doi.org/10.1039/C6TA06078A.

[84] Y. Li, B. Hu, C. Xia, W.Q. Xu, J.P. Lemmon, F. Chen, A Novel Fuel Electrode Enabling Direct CO2 Electrolysis with Excellent and Stable Cell Performance, J. Mater. Chem. A 5 (39) (2017) 20833–20842, https://doi.org/10.1039/C7TA05750D.

[85] X. Meng, Y. Wang, Y. Zhao, T. Zhang, N. Yu, X. Chen, M. Miao, T. Liu, In-Situ Exsolution of Nanoparticles from Ni Substituted Sr2Fe1.5Mo0.5O6 Perovskite Oxides with Different Ni Doping Contents, Electrochim. Acta 348 (2020), 136351, https://doi.org/10.1016/j.electacta.2020.136351.

[86] K. Zhu, T. Wu, M. Li, R. Lu, X. Zhu, W. Yang, Perovskites Decorated with Oxygen Vacancies and Fe–Ni Alloy Nanoparticles as High-Efficiency Electrocatalysts for the Oxygen Evolution Reaction, J. Mater. Chem. A 5 (37) (2017) 19836–19845, https://doi.org/10.1039/C7TA05404A.

[87] X. Zhang, Y. Tong, T. Liu, D. Zhang, N. Yu, J. Zhou, Y. Li, X.-K. Gu, Y. Wang, Robust Ruddlesden-Popper Phase Sr3Fe1.3Mo0.5Ni0.2O7-δ Decorated with in-Situ Exsolved Ni Nanoparticles as an Efficient Anode for Hydrocarbon Fueled Solid Oxide Fuel Cells, SusMat 2 (4) (2022) 487–501, https://doi.org/10.1002/sus2.58.

[88] S. Hu, L. Zhang, H. Liu, W. Li, Z. Cao, L. Cai, Y. Zhu, X. Zhu, W. Yang, Detrimental Phase Evolution Triggered by Ni in Perovskite-Type Cathodes for CO2 Electroreduction, Journal of Energy Chemistry 36 (2019) 87–94, https://doi.org/10.1016/j.jechem.2019.06.001.

[89] N. Hou, T. Yao, P. Li, X. Yao, T. Gan, L. Fan, J. Wang, X. Zhi, Y. Zhao, Y. Li, A-Site Ordered Double Perovskite with in Situ Exsolved Core-Shell Nanoparticles as Anode for Solid Oxide Fuel Cells, ACS Appl. Mater. Interfaces 11 (7) (2019) 6995–7005, https://doi.org/10.1021/acsami.8b19928.

[90] T. Tan, Z. Wang, M. Qin, W. Zhong, J. Hu, C. Yang, Liu M. In Situ Exsolution of Core-Shell Structured NiFe/FeOx Nanoparticles on Pr0.4Sr1.6(NiFe)1.5Mo0.5O6-δ for CO2 Electrolysis, Adv. Funct. Mater. 32 (34) (2022) 2202878, https://doi.org/10.1002/adfm.202202878.

[91] X. Wu, Y. Yu, Y. Chen, L. Li, Z.-F. Ma, Y.-M. Yin, Construction of Multifunctional Nanoarchitectures in One Step on a Composite Fuel Catalyst through In Situ Exsolution of La0.5Sr0.5Fe0.8Ni0.1Nb0.1O3−δ. *ACS Appl*, Mater. Interfaces 12 (31) (2020) 34890–34900, https://doi.org/10.1021/acsami.0c08016.

[92] J.H. Kim, J.K. Kim, J. Liu, A. Curcio, J.-S. Jang, I.-D. Kim, F. Ciucci, W. Jung, Nanoparticle Ex-Solution for Supported Catalysts: Materials Design, Mechanism and Future Perspectives. *ACS Nano* 15 (1) (2021) 81–110, https://doi.org/10.1021/acsnano.0c07105.

[93] D. Neagu, V. Kyriakou, I.-L. Roiban, M. Aouine, C. Tang, A. Caravaca, K. Kousi, I. Schreur-Piet, I.S. Metcalfe, P. Vernoux, M.C.M. van de Sanden, M.N. Tsampas, In Situ Observation of Nanoparticle Exsolution from Perovskite Oxides: From Atomic Scale Mechanistic Insight to Nanostructure Tailoring, ACS Nano 13 (11) (2019) 12996–13005, https://doi.org/10.1021/acsnano.9b05652.

[94] M. Sase, K. Yashiro, K. Sato, J. Mizusaki, T. Kawada, N. Sakai, K. Yamaji, T. Horita, H. Yokokawa, Enhancement of Oxygen Exchange at the Hetero Interface of (La, Sr) CoO3/(La, Sr)2CoO4 in Composite Ceramics, Solid State Ion. 178 (35) (2008) 1843–1852, https://doi.org/10.1016/j.ssi.2007.11.039.

[95] J.W. Han, B. Yildiz, Mechanism for Enhanced Oxygen Reduction Kinetics at the (La, Sr)CoO3−δ/(La, Sr)2CoO4+δ Hetero-Interface, Energ. Environ. Sci. 5 (9) (2012) 8598–8607, https://doi.org/10.1039/C2EE03592H.